Supporting Information

for

Structure elucidation of a complex CO_2-based organic framework material by NMR crystallography

Julien Leclaire,*[ab] Guillaume Poisson,[ab] Fabio Ziarelli,[c] Gerard Pepe,[d] Frédéric Fotiadu,[b] Federico M. Paruzzo,[f] Aaron J. Rossini,[e,f] Jean-Nicolas Dumez,‡[e] Bénédicte Elena-Herrmann*[e] and Lyndon Emsley[f]

Content

1. General methods

1.1. Solvents

All solvents were purified by standard procedures or obtained from a Solvent Purification System (Braun SPS 800).

1.2. Synthesis

^{15}N-labeled DETA[1], dynamat **DM$^{A}_{2}$(CO$_2$)** and **DM$^{A}_{2}$(CO$_2$)***,[2] were synthesized according to reported procedures.

1.3. Nuclear Magnetic Resonance

1.3.1 Room temperature NMR experiments

Solid-State NMR experiments were performed on a 9.4 T Bruker Avance III spectrometer equipped with a widebore 4mm triple resonance CP-MAS Bruker probehead (^{15}N-^{13}C double CP experiment), a 11.7 T Bruker Avance III spectrometer equipped with a standard 4 mm double resonance CP-MAS probe (^{13}C-^{13}C INADEQUATE experiment) and a 18.8 T Bruker Avance III spectrometer equipped with either a 3.2 mm (for ^{1}H-^{15}N solid-state refocused) or a 1.3 mm (for ^{1}H-^{13}C dipolar HETCOR) standard triple resonance CP-MAS probe. The sample temperature was regulated at 293 K. For all CP experiments the amplitude of the ^{1}H *rf* field was ramped during the contact time. SPINAL-64 decoupling was applied during ^{13}C acquisition and echo delays in refocused INADEQUATE experiments. The two dimensional ^{1}H-^{15}N refocused INEPT scalar correlation and ^{1}H-^{13}C dipolar HETCOR experiments were carried out on a sample with uniform ^{15}N isotope labeling and selective ^{13}C labeling on the carboxyl resonances ([U-^{15}N, ^{13}CO] labeled **DM$^{A}_{2}$(CO$_2$)***).

1.3.2 DNP-enhanced NMR experiments

All DNP-enhanced solid-state NMR experiments were performed on a 9.4 T Bruker Avance III solid-state NMR spectrometer which was equipped with a 3.2 mm triple resonance

low temperature MAS probe, a Bruker Biospin low temperature cooling cabinet and a 263 GHz gyrotron microwave source.[3] The samples were cooled to ca. 100 K. The sweep coil of the main magnetic field ($\nu_0(^1H)$ = 400.075 MHz) was set so that microwave (μwave) irradiation occurred at the same position as the ε maximum for TOTAPOL.[4] The estimated power of the μwave beam at the output of the waveguide was ca. 5 W. The sample spinning frequency (ν_{rot}) was between 8000 - 10000 Hz in all cases. For all CP experiments the amplitude of the ^1H rf field was ramped during the contact time to improve efficiency.[5] The proton DNP enhancement (ε) was measured by comparing the intensity of proton spin echo spectra acquired with and without μwave irradiation.

Samples of **$DM^A_2(CO_2)$** were prepared for DNP solid-state NMR experiments by impregnating ca. 34 mg of the as synthesized powdered **$DM^A_2(CO_2)$** with 20 μL of 16 mM TEKPol [6] tetrachloroethane solution. The impregnated **$DM^A_2(CO_2)$** material was mixed with a glass stir rod to uniformly distribute the radical solution, then transferred to a 3.2 mm thin wall zirconium oxide rotor. The particulate solid material was externally polarized by proton spin diffusion of enhanced polarization from the particle surface.[7,8] We observed a proton DNP enhancement (ε_H) of ca. 230 for the solvent at the surface of the particles (as measured with a ^1H spin echo experiment). A proton DNP enhancement of ca. 37 was measured for the protons within the macro nano-/micro-particles by comparing the intensity of ^{13}C CPMAS spectra acquired with and without microwave irradiation to drive DNP (spectra were acquired with a polarization delay of 13 s). The ratio of surface and interior proton DNP enhancements is consistent with the intermediate proton T_1 of ca. 28 s that was measured for the material [9]

1.4. X-ray diffraction measurement

The diffraction spectra were obtained using an Inel CPS-120 x-ray powder diffractometer with the wavelength 1.5418Å (Cu Kα).

1.5. Modelling

1.5.1. Virtual Crystal Generation

For virtual crystal generation and pre-selection, the molecules were treated as rigid bodies in both steps. The software used for the first step, GenMol, based on molecular mechanics [10], has its own empirical force field and uses the Dell Ré method (semi-empirical approximation [11], [12] for atomic charge calculation. Crystal were generated from **1-6** in the space group of highest probability corresponding to a monoclinic packing mode (group P1) in agreement with previous analyses. 10000 lattices were first produced in order to find the most probable packing modes (which are strongly correlated to the geometrical features of the oligodynablocks). Crystals were then generated by randomly combining lattice, positional and rotational parameters within the lattice using the genetic algorithm (to avoid any edge effect, spherical crystals of 120 Å diameter were generated). The three "genes" which are screened consist in one lattice being randomly chosen among the 10000 generated combined with a set of positional and rotational parameters of the oligodynablock in the lattice ("centroid" position: xc, yc, zc and orientation Rx, Ry, Rz). 100 crystals are generated from 300 possible genes and their energy calculated. The most stable virtual crystal of the series is then conserved as a potential hit. The same process is conducted 300 times by using genes that were not previously tested, leading to 300 virtual crystal candidates. As a second step of the process, these 300 structures are then energetically optimized using the algorithm *steepest descent,* by varying the positional values of the molecule and the lattice parameters around the initial solution. After this round of optimization, structures are ranked according to their crystal energy value (from lowest to highest). PXRD spectra of these 300 structures are generated with Plato software [13] and compared to the experimental spectrum. The first ranking criteria is the crystal energy value. When structures displaying high stability (< -180 kcal) were obtained all were conserved as potential hits for the subsequent step of DFT calculations (dynablocks **2** & **6**).

1.5.2. DFT calculation

Geometry optimization and chemical shift calculations were carried out with the plane-wave DFT code CASTEP [14] using the generalized gradient approximation (GGA) functional PBE [15] and Vanderbilt-type ultrasoft pseudopotentials [16]. The first Brillouin zone was sampled according to the scheme proposed by Monkhorst and Pack [17]. NMR shieldings were calculated using the gauge- including projector augmented-wave method (GIPAW) method [18]. The geometry optimizations and NMR calculations used a maximum cut-off energy of 550 eV. A grid of k-points corresponding to a maximum spacing of 0.05 Ã-1 in reciprocal space was used for NMR calculations. A single k-point was used for geometry optimisation. All atom positions were optimised, with fixed cell parameters.

Calculated chemical shieldings $\sigma_{\square}$ were converted into calculated chemical shifts $\delta_{\square}$ using the relation $\delta_i = \sigma_{ref} - \sigma_i$ with the values of σ_{ref} calculated to equate the average calculated shift and average experimental shift. The actual values σ_{ref} for ^{1}H, ^{13}C and ^{15}N are given for each candidate structure in the respective table caption in section 2.2.

2. Individual datasets

2.1. Experimental data

2.1.1. PXRD

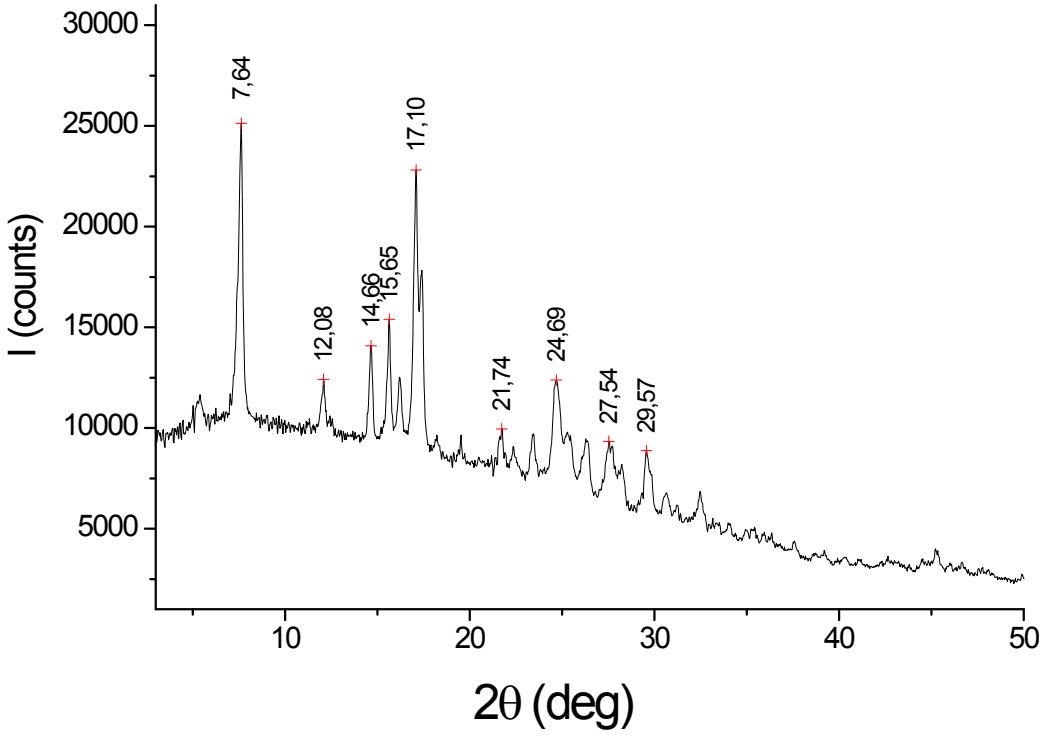

Figure S1: Powder X-ray diffraction spectrum of the dynamat $\mathbf{DM^{A}_{2}(CO_{2})}$ recorded under at 300 K.

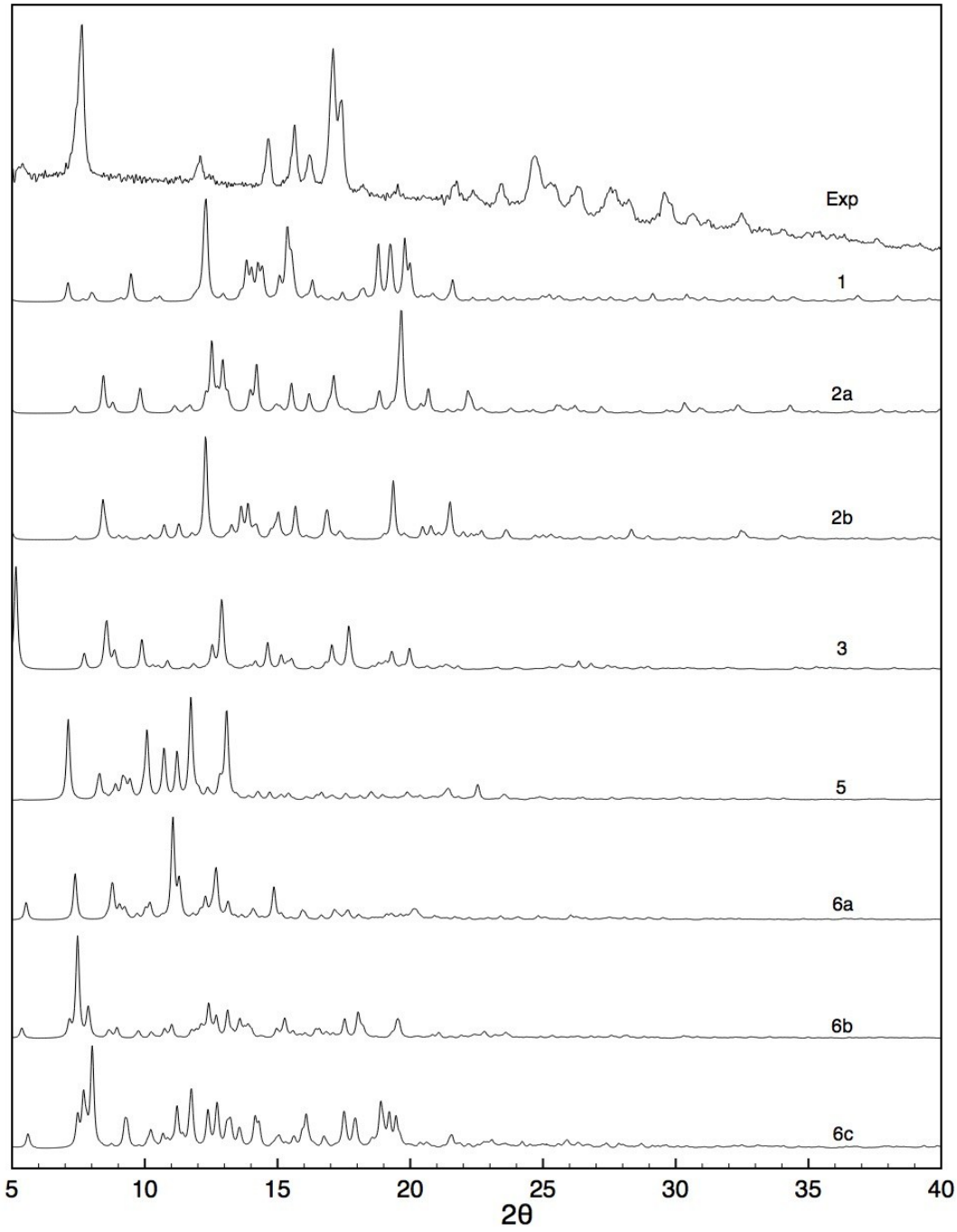

Figure S2: Simulated PXRD spectra for candidate structures **1**-**6c** before all-atom DFT optimization. Experimental spectrum is given for comparison

2.1.2. NMR experiments

2.1.2.a. ^{15}N-^{13}C double CP experiment

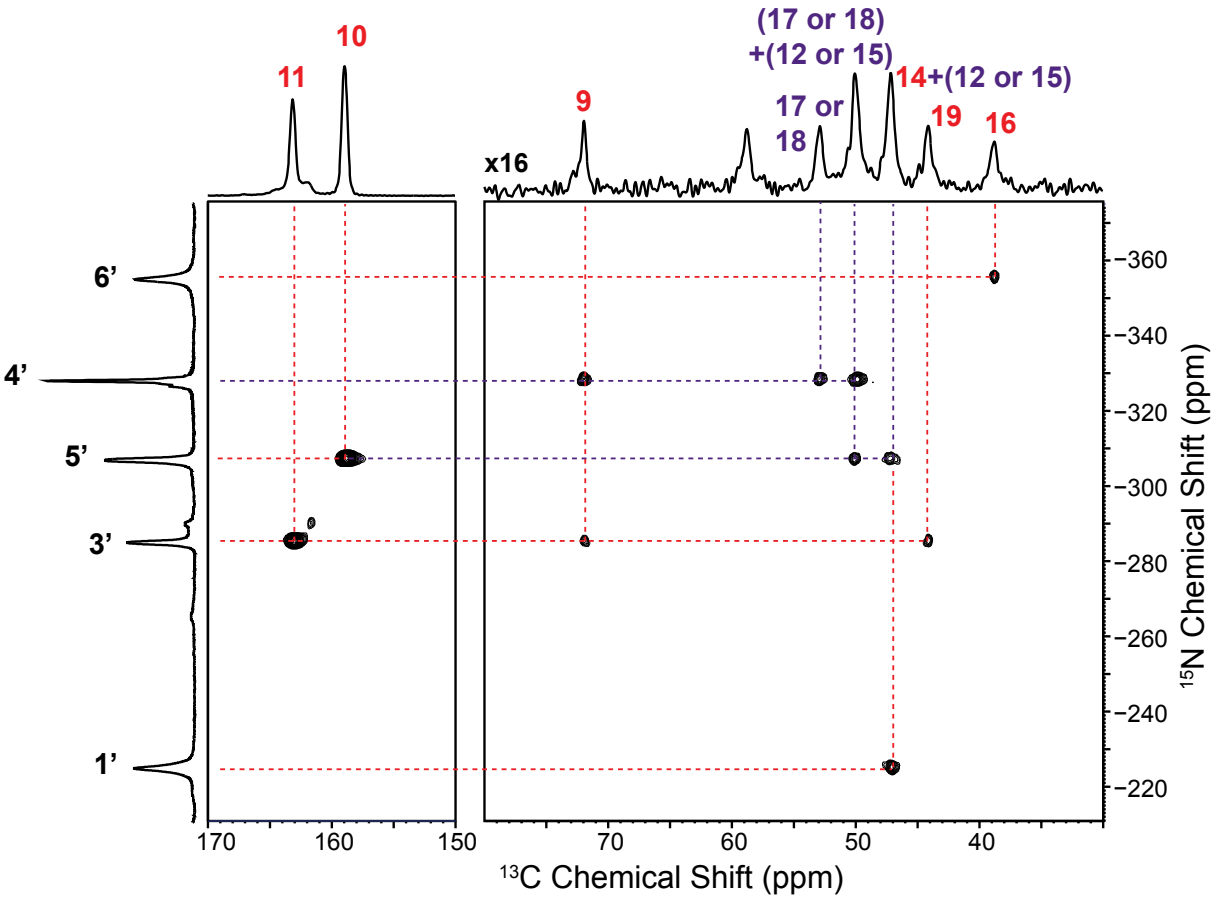

Figure S3: ^{15}N-^{13}C 2D HETCOR spectrum of the [^{15}N, $^{13}CO_2$] labeled dynamic material **$DM^A_2(CO_2)$***. The experiment was performed using the double cross-polarization (CP) magic-angle spinning (MAS) pulse sequence developed by Schaefer *et al.* [19]. In this $^{13}C/^{15}N$ chemical shift correlation, the ^{1}H coherence is transferred to ^{15}N during the first CP period (3.5ms). Then, the ^{15}N chemical shift is allowed to evolve, and the ^{15}N coherence is subsequently transferred to ^{13}C during the second CP period (1ms) for observation. Due to high spinning rate dependence of this second CP transfer, the spinning rate was set exactly at 7000Hz.

2.1.2.b. ^{1}H-^{13}C dipolar HETCOR

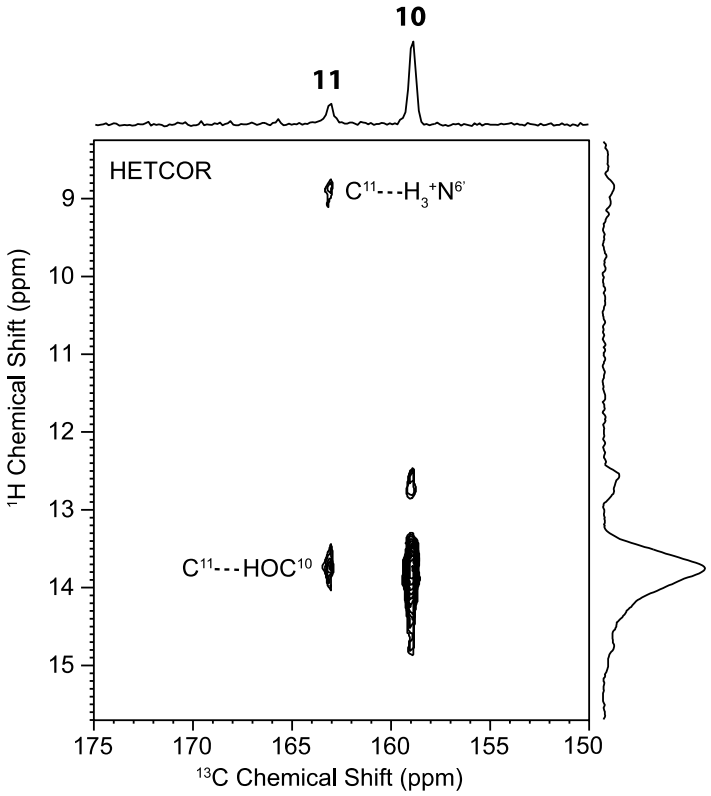

Figure S4: ^{1}H-^{13}C dipolar HETCOR spectrum of **DM$^{A}_{2}$(CO$_2$)***, acquired at a sample spinning rate of 60 kHz. The spectrum was obtained with 32 scans per increment, 256 t_1 increments of 35.7 μs each, and a recycle delay of 2.5s (< 6 hours total experimental time). A contact time of 2 ms was employed for ^{1}H-^{13}C cross polarization transfer, and low power TPPM decoupling was used during ^{13}C acquisition. The STATES procedure was used for quadrature detection in F_1.

2.1.2.c. ^{1}H-^{15}N solid-state refocused INEPT

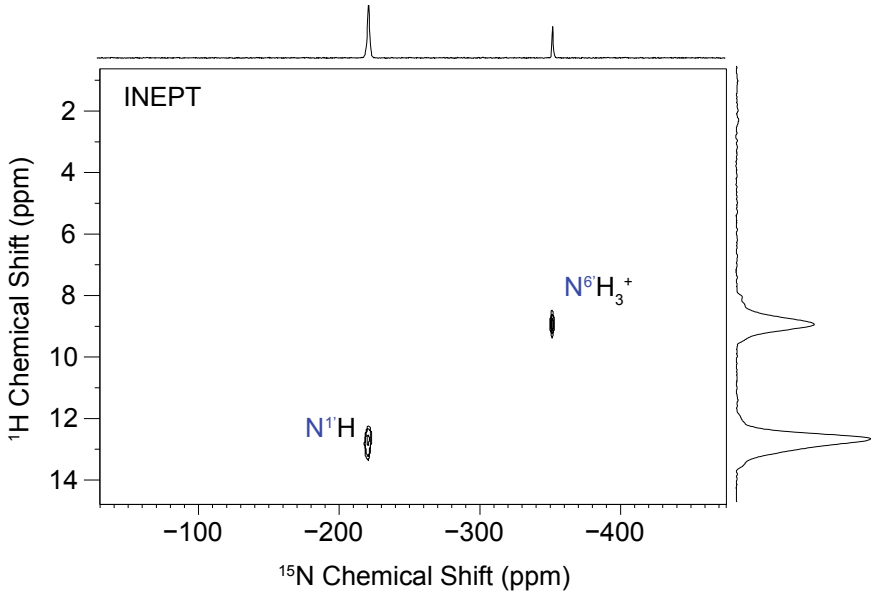

Figure S5: ^{1}H-^{15}N solid-state refocused INEPT (scalar correlation) spectrum of **DM$^{A}_{2}$(CO$_2$)***, acquired at a sample spinning rate of 22321 Hz. The spectrum was obtained with 96 scans per increment, 160 t_1 increments of 128 μs each, and a recycle delay of 3s (13 hours total experimental time). Four 2.24 ms τ/4 delays were employed for the INEPT through-bond heteronuclear coherence transfer and ^{1}H homonuclear dipolar decoupling was achieved during the INEPT and t_1 evolution times using the eDUMBO-1$_{22}$ scheme with a 32 μs period and 100 kHz proton decoupling frequency. The STATES-TPPI procedure was used for quadrature detection in F_1.

2.1.2.d. ^{13}C-^{13}C refocused INADEQUATE at room temperature with conventional solid-state NMR.

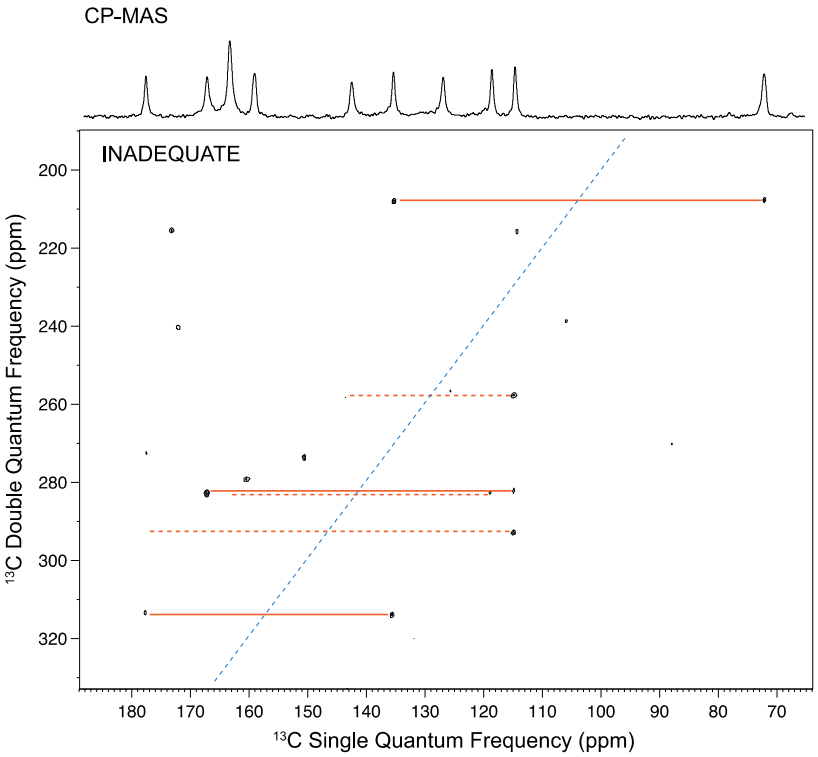

Figure S6: ^{13}C-^{13}C refocused INADEQUATE scalar correlation spectrum (aromatic region) of natural abundance **$DM^{A}_{2}(CO_2)$** acquired with a sample spinning rate of 12.5 kHz and a carbon resonance frequency of 125.75 MHz. The spectrum was obtained with 1024 scans per increment, 160 t_1 increments for a 260 ppm spectral width in F_1, and a recycle delay of 2.5 s (114 hours total experimental time). Four 3.6 ms τ/4 delays were employed for generation and reconversion of DQ coherences. The TPPI procedure was used for quadrature detection in F_1. The corresponding standard CP-MAS spectrum acquired under equivalent condition is display on top of the 2D INADEQUATE map. Observed carbon-carbon correlations are indicated with red lines. Dotted lines are used when only one of the two expected correlation signals is visible.

2.1.2.e. DNP-enhanced ^{13}C-^{13}C INADEQUATE.

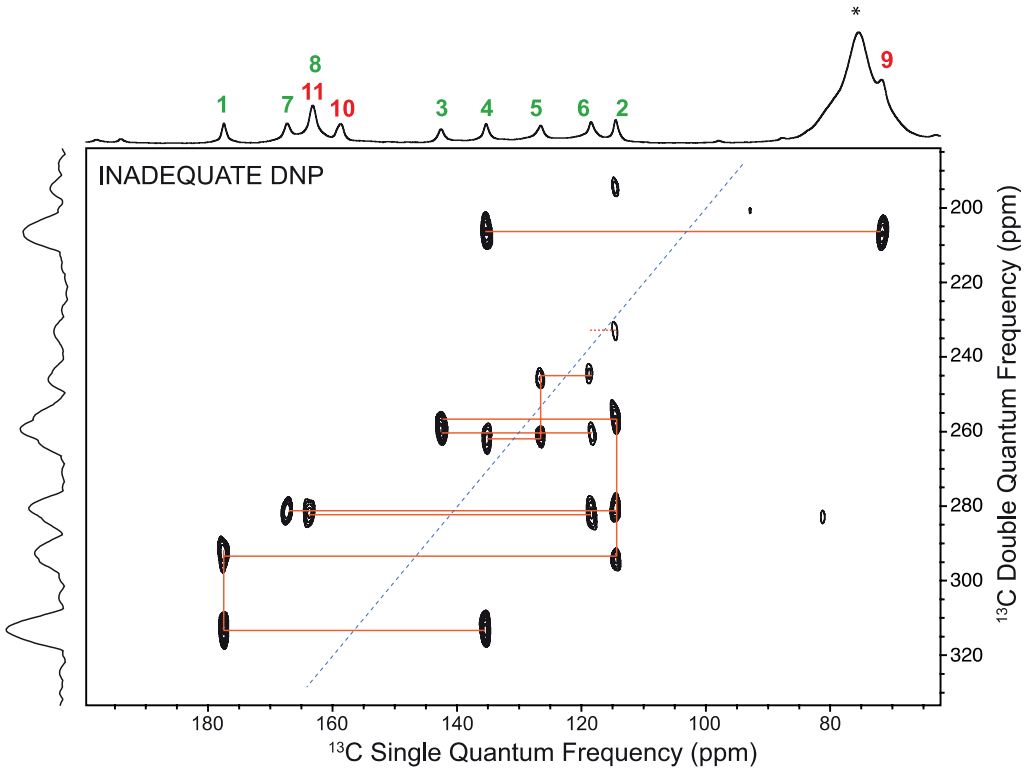

Figure S7: DNP-enhanced ^{13}C-^{13}C refocused INADEQUATE scalar correlation spectrum (zoom on aromatic region) of natural abundance **$DM^A_2(CO_2)$** acquired with a sample spinning rate (ν_{rot}) of 10 kHz. Visible carbon-carbon correlations are indicated with red lines. Artifacts and solvent signals are marked with asterisks. The spectrum was obtained with 32 scans per increment, 62 t_1 increments, a 28.0 µs t_1 increment and a 30.0 s recycle delay (16.5 hours total experiment time). SPINAL64 decoupling[8] was applied during acquisition and echo delays. Four 3 ms τ/4 delays were employed for generation and reconversion of DQ coherences. The STATES-TPPI procedure was used to attain quadrature detection in F_1. The DNP enhanced ^{13}C CPMAS spectrum is shown at the top of the 2D spectrum.

2.1.2.f. Short range DNP-enhanced 1H-13C LG-CP HETCOR experiment

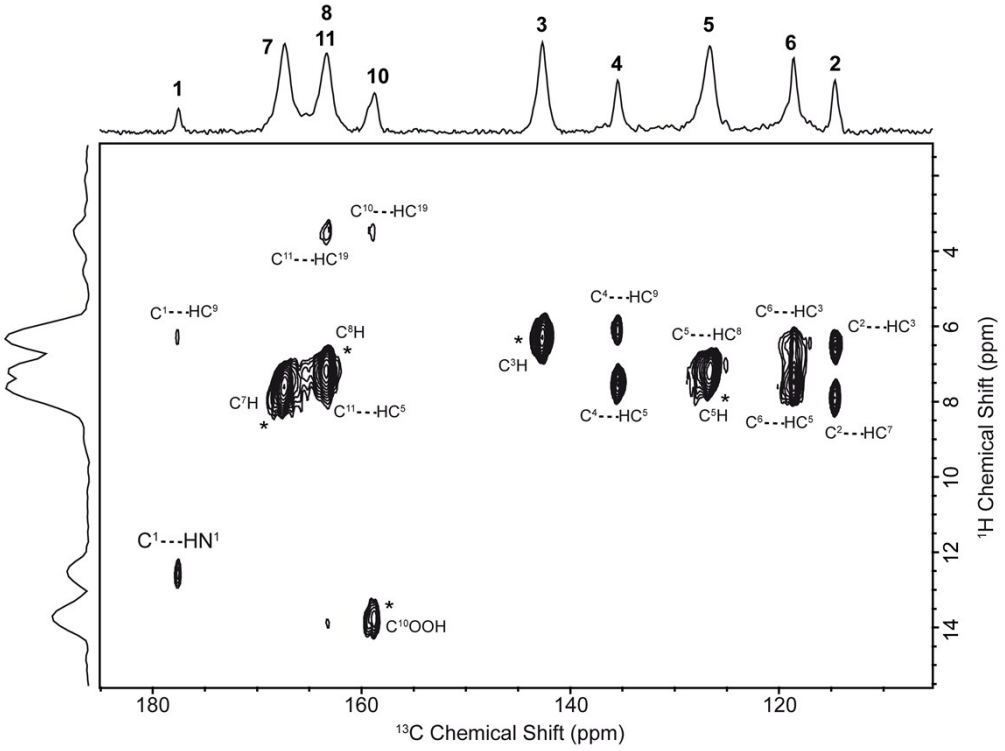

Figure S8: Short range DNP-enhanced ^{1}H-^{13}C LG-CP HETCOR spectrum of natural abundance **DM$^{A}_{2}$(CO$_2$)**. The magic-angle spinning frequency was set to 12.5 kHz. Lee-Goldberg cross-polarization with 250 μs contact time was used to transfer magnetization from ^{1}H to ^{13}C. The spectrum was acquired with 4 scans per each of the 128 t_1 increments, with t_1 incremented in steps of 64 μs and 6s recycle delay. SPINAL64 decoupling was applied during acquisition. The STATES-TPPI procedure was used to attain quadrature detection in F_1.

2.1.2.g. DNP-enhanced ^{13}C MAT spectrum for measurement of chemical shift anisotropies

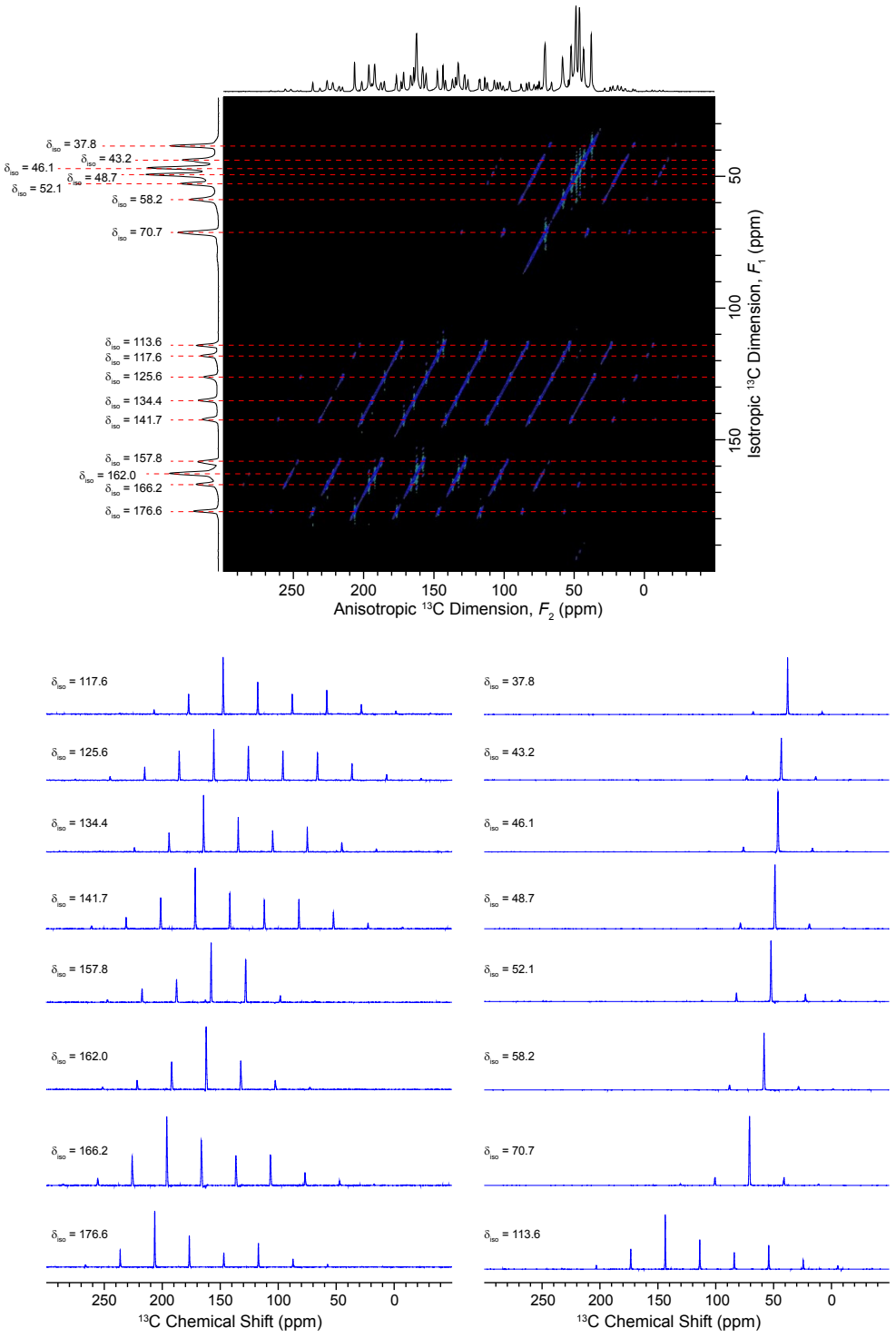

Figure S9. DNP enhanced ^{13}C magic angle turning (MAT) spectrum of natural abundance **$DM^{A}_{2}(CO_2)$**, correlating isotropic ^{13}C chemical shifts to their (anisotropic and isotropic) spinning side band manifolds. The 2D spectrum was acquired with a 3000 Hz MAS frequency, 28 scans per increment, a 6.0 s recycle delay and 360 individual t_1 increments, with t_1 incremented in steps of 46.30 μs (16.8 hours total acquisition). The sideband manifolds for each isotropic chemical shift are shown in the lower portion of the figure. CS tensor parameters were obtained by extracting the sideband manifolds of each site from the 2D spectrum, then fitting the sideband manifold intensities with the HBA-Graphic Analysis Program v1.7.3 (Dr. K. Eichele, University of Tubingen). The constant time five-pi pulse MAT experiment of Grant and co-workers was employed for acquisition of the MAT spectrum [20].

2.1.2. NMR experimental chemical shifts

^{1}H	δ (ppm)	^{13}C	δ_{iso} (ppm)	Aniso (ppm)	Asymmetry	^{15}N	δ (ppm)
C10OOH	13.8	C1	177.6	-158.46	0.08	N2'	-89
N1'H	12.68	C7	167.4	-157.99	0.57	N1'	-221.4
N6'H	8.96	C8	163.4	93.36	0.96	N3'	-281.8
C7H	7.76	C11	163.3	93.36	0.96	N5'	-304
C8H	7.46	C10	158.8	109.35	0.41	N4'	-325
C5H	7.43	C3	142.7	-175.13	0.61	N6'	-352.4
C3H	6.3	C4	135.6	-157.00	0.42		
C9H	6.02	C5	126.7	-178.34	0.71		
C12H	4	C6	118.6	-161.09	0.41		
C19H	3.92	C2	114.7	-163.85	0.34		
C13H	3.8	C9	72.5	-48.61	0.98		
C16H	3.6	C13	59.2	-46.47	0.02		
C15H	3.4	C18	53.2	-54.42	0.75		
C18H	3.23	C17	49.4	-44.94	0.60		
C14H	3.04	C12	49.9	-44.94	0.60		
C17H	2.88	C15	47.3	-44.03	0.16		
		C14	47.3	-44.03	0.16		
		C19	44.3	-47.77	0.44		
		C16	38.9	-37.83	0.00		

Table S1: Experimental NMR chemical shifts of **$DM^{A}_{2}(CO_2)$**, as determined from the set of complementary NMR experiments described above.

2.2. Simulated data

2.2.1. Virtual crystal 1

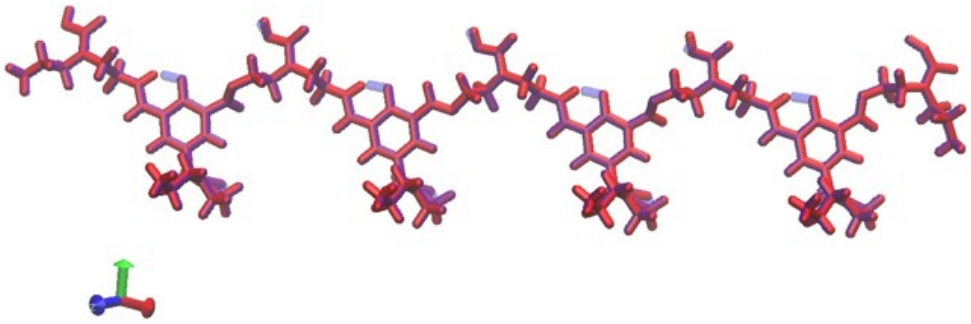

Figure S10: molecular model of the oligodynablock corresponding to virtual crystal **1** before (blue) and after (red) QM refinement

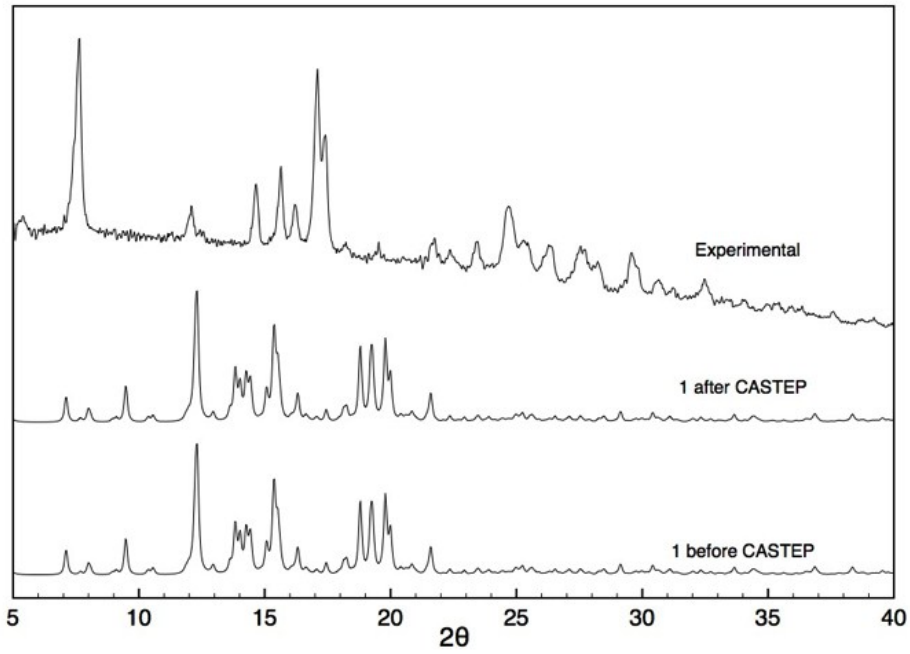

Figure S11 : PXRD spectrum of virtual crystal **1** before and after QM refinement

^{1}H	δ (ppm)	^{13}C	δ_{iso} (ppm)	^{15}N	δ (ppm)
C10OOH	10.10	C1	182.21	N2'	-51.59
N1'H	6.60	C7	160.55	N1'	-240.56
N6'H	8.24	C8	164.02	N3'	-274.27
C7H	5.57	C11	153.09	N5'	-299.46
C8H	6.56	C10	151.76	N4'	-324.90
C5H	9.28	C3	139.51	N6'	-382.83
C3H	9.31	C4	128.15		
C9H	5.06	C5	135.22		
C12H	5.10	C6	133.44		
C19H	5.15	C2	118.61		
C13H	6.39	C9	78.12		
C16H	2.69	C13	62.04		
C15H	4.65	C18	47.93		
C18H	4.39	C17	54.05		
C14H	5.28	C12	50.64		
C17H	4.05	C15	48.85		
		C14	45.81		
		C19	45.18		
		C16	31.75		

Table S3: NMR chemical shifts of virtual structure **1**, from CASTEP calculation (chemical shielding references: σ_{ref}^{1H}=32.26; σ_{ref}^{13C}=170.24; σ_{ref}^{15N}=-158.38).

2.2.2. Virtual crystal 2a

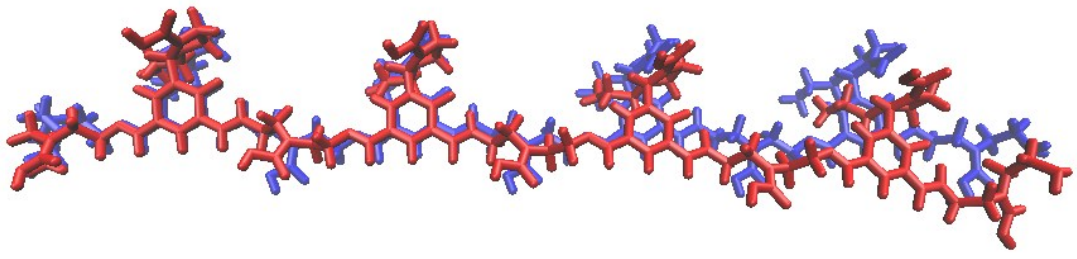

Figure S12 : molecular model of the oligodynablock corresponding to virtual crystal **2a** before (blue) and after (red) QM refinement

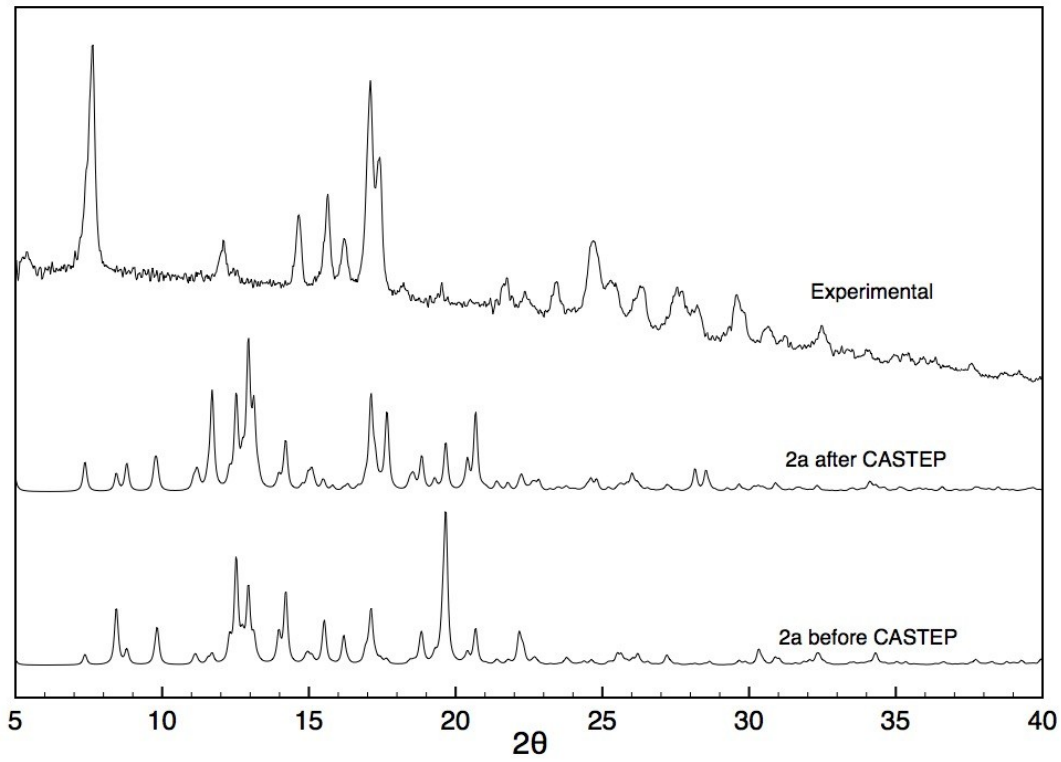

Figure S13 : PXRD spectrum of virtual crystal **2a** before and after QM refinement

^{1}H	δ (ppm)	^{13}C	δ_{iso} (ppm)	Aniso (ppm)	Asymmetry	^{15}N	δ (ppm)
C10OOH	13.80	C1	180.77	-154.25	0.26	N2'	-52.00
N1'H	12.68	C7	161.03	-134.22	0.73	N1'	-231.46
N6'H	8.96	C8	161.22	139.01	0.56	N3'	-275.70
C7H	7.76	C11	155.21	110.60	0.16	N5'	-292.47
C8H	7.46	C10	155.42	120.50	0.13	N4'	-321.52
C5H	7.43	C3	137.44	-163.21	0.69	N6'	-363.45
C3H	6.30	C4	134.74	-153.73	0.43		
C9H	6.02	C5	136.51	-177.07	0.87		
C12H	4.00	C6	123.15	-165.81	0.38		
C19H	3.92	C2	117.31	-169.32	0.26		
C13H	3.80	C9	78.55	23.77	0.31		
C16H	3.60	C13	60.89	-61.73	0.28		
C15H	3.40	C18	51.99	-62.86	0.36		
C18H	3.23	C17	45.25	-58.70	0.53		
C14H	3.04	C12	49.46	-55.95	0.57		
C17H	2.88	C15	48.10	-47.07	0.46		
		C14	49.42	-51.72	0.70		
		C19	44.80	-38.96	0.62		
		C16	39.59	-2.29	0.81		

Table S5: NMR chemical shifts of virtual structure **2a**, from CASTEP calculation (chemical shielding references: σ_{ref}^{1H}=31.0; σ_{ref}^{13C}=167.79; σ_{ref}^{15N}=-158.61).

2.2.3. Virtual crystal 2b

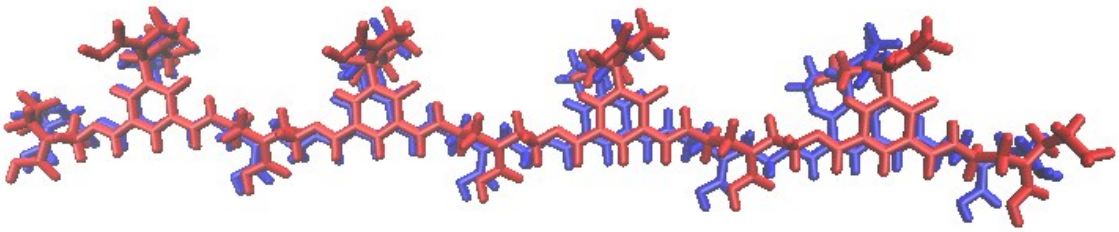

Figure S14 : molecular model of the oligodynablock corresponding to virtual crystal **2b** before (blue) and after (red) QM refinement

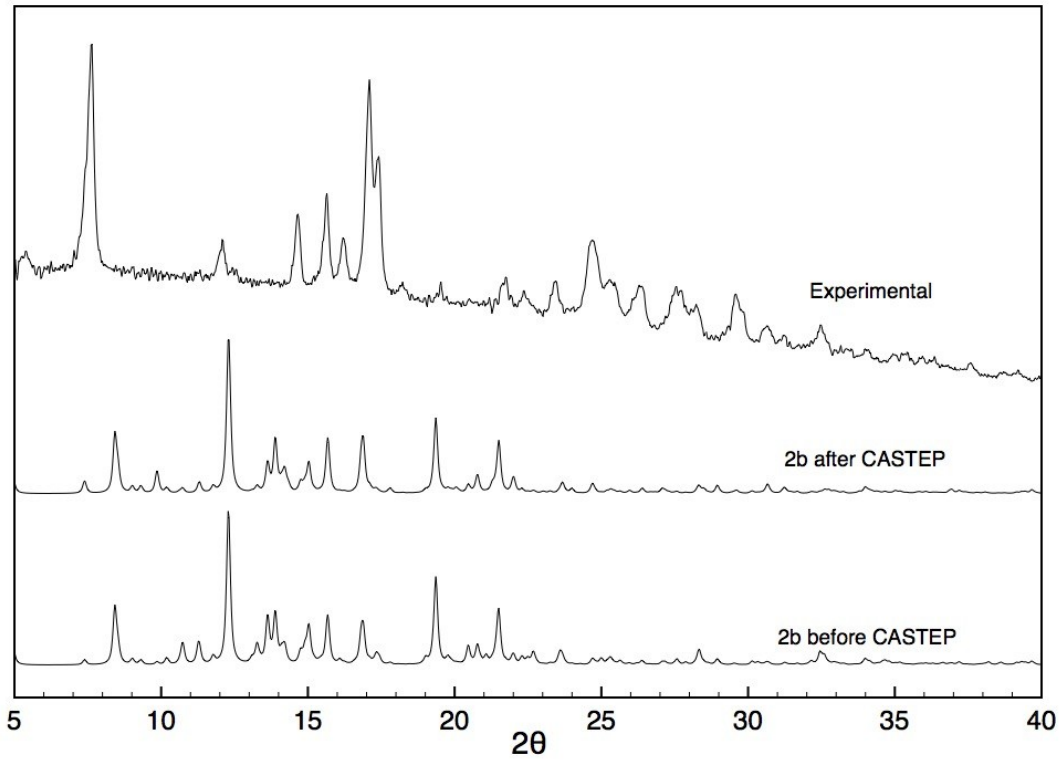

Figure S15 : PXRD spectrum of virtual crystal **2b** before and after QM refinement

^{1}H	δ (ppm)	^{13}C	δ_{iso} (ppm)	Aniso (ppm)	Asymmetry	^{15}N	δ (ppm)
C10OOH	13.12	C1	180.88	-152.47	0.27	N2'	-45.66
N1'H	14.07	C7	161.52	-34.60	0.60	N1'	-232.16
N6'H	5.75	C8	159.64	13.23	0.54	N3'	-268.40
C7H	7.71	C11	157.36	-31.01	0.56	N5'	-299.07
C8H	9.20	C10	155.83	-21.35	0.49	N4'	-325.59
C5H	8.18	C3	135.41	-111.75	0.71	N6'	-359.77
C3H	7.14	C4	132.91	-35.81	0.60		
C9H	5.28	C5	139.99	6.59	0.29		
C12H	2.99	C6	123.49	28.61	0.48		
C19H	4.26	C2	117.65	-167.84	0.26		
C13H	3.91	C9	80.07	-37.46	0.60		
C16H	3.18	C13	57.69	54.87	0.39		
C15H	3.23	C18	51.68	-34.74	0.48		
C18H	3.94	C17	45.18	-80.82	0.56		
C14H	3.28	C12	49.49	-103.29	0.55		
C17H	3.02	C15	47.48	78.61	0.53		
		C14	48.03	-49.30	0.44		
		C19	45.79	-76.76	0.64		
		C16	40.72	-43.65	0.64		

Table S7: NMR chemical shifts of virtual structure **2b**, from CASTEP calculation (chemical shielding references: σ_{ref}^{1H}=30.95; σ_{ref}^{13C}=168.1; σ_{ref}^{15N}=-156.8).

2.2.4. Virtual crystal 3

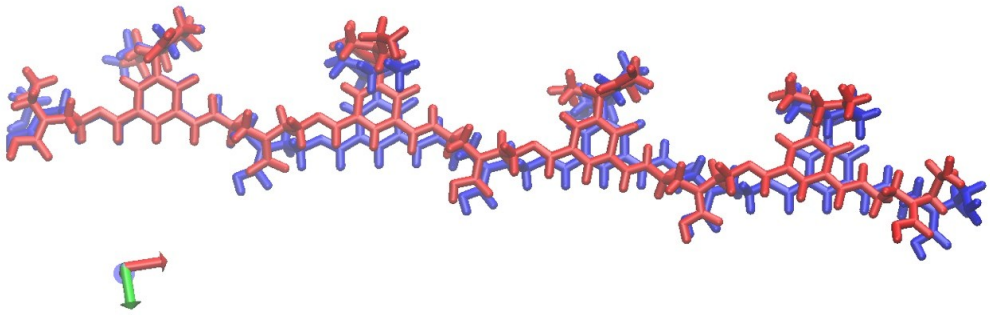

Figure S16 : molecular model of the oligodynablock corresponding to virtual crystal **3** before (blue) and after (red) QM refinement

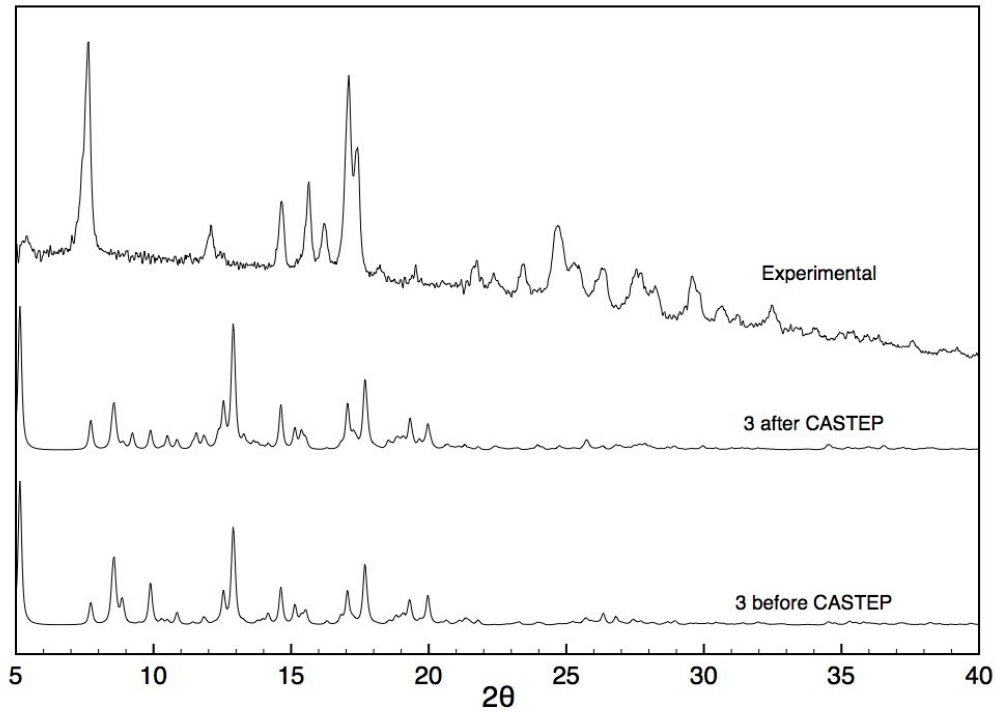

Figure S17: PXRD spectrum of virtual crystal **3** before and after QM refinement

^{1}H	δ (ppm)	^{13}C	δ_{iso} (ppm)	Aniso (ppm)	Asymmetry	^{15}N	δ (ppm)
C10OOH	11.66	C1	181.53	-154.35	0.26	N2'	-56.18
N1'H	15.43	C7	161.26	-134.65	0.77	N1'	-239.53
N6'H	6.28	C8	162.70	139.23	0.46	N3'	-281.40
C7H	7.94	C11	155.35	115.43	0.10	N5'	-301.96
C8H	7.97	C10	158.57	112.05	0.33	N4'	-332.70
C5H	7.90	C3	137.82	-160.26	0.71	N6'	-361.58
C3H	7.12	C4	135.44	-155.49	0.41		
C9H	5.97	C5	135.08	-184.82	0.77		
C12H	3.23	C6	125.22	-168.26	0.38		
C19H	4.24	C2	117.13	-170.00	0.24		
C13H	3.83	C9	75.57	-10.66	0.54		
C16H	3.23	C13	60.21	-71.65	0.28		
C15H	3.56	C18	51.97	-57.98	0.63		
C18H	3.78	C17	46.83	-58.72	0.58		
C14H	3.36	C12	49.17	-27.75	0.46		
C17H	2.78	C15	46.68	-53.74	0.39		
		C14	45.50	-61.16	0.56		
		C19	45.26	-40.31	0.76		
		C16	38.59	-39.25	0.54		

Table S9: NMR chemical shifts of virtual structure **3**, from CASTEP calculation (chemical shielding references: σ_{ref}^{1H}=31.03; σ_{ref}^{13C}=169.05; σ_{ref}^{15N}=-162.27).

2.2.5. Virtual crystal 5

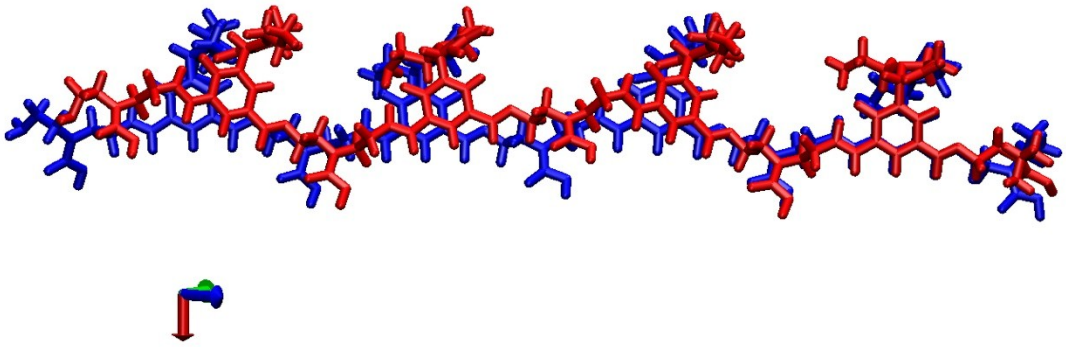

Figure S18 : molecular model of the oligodynablock corresponding to virtual crystal **5** before (blue) and after (red) QM refinement

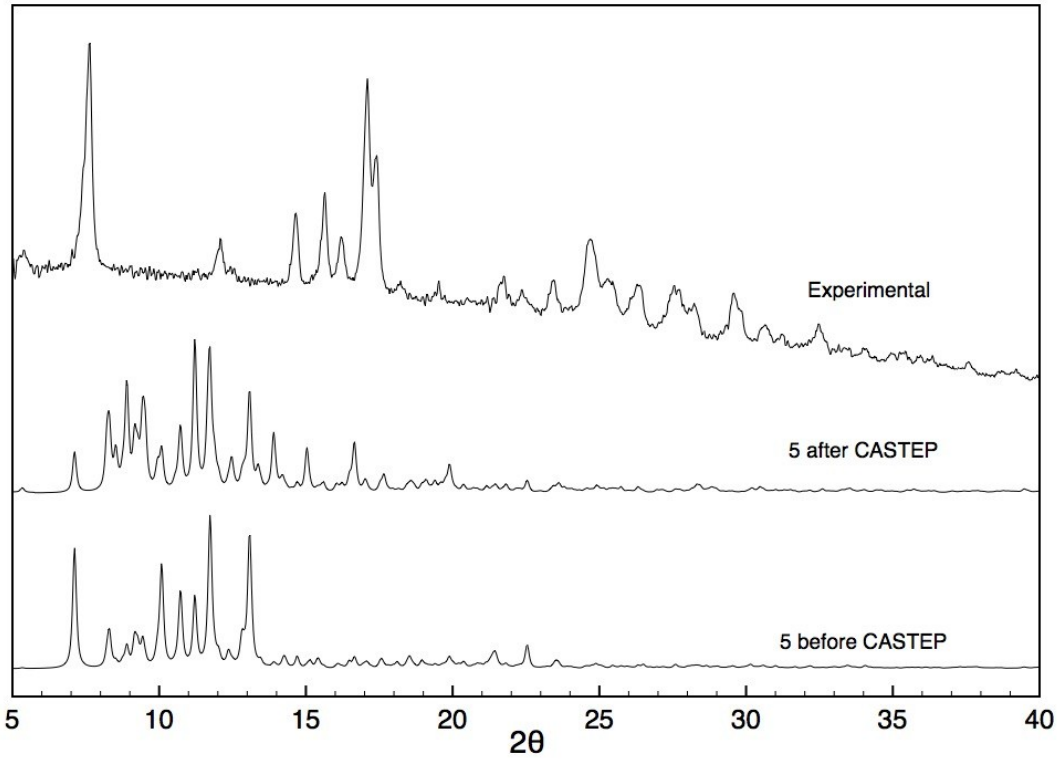

Figure S19 : PXRD spectrum of virtual crystal **5** before and after QM refinement

^{1}H	δ (ppm)	^{13}C	δ_{iso} (ppm)	Aniso (ppm)	Asymmetry	^{15}N	δ (ppm)
C10OOH	10.97	C1	182.73	-27.51	0.39	N2'	-57.79
N1'H	16.36	C7	160.88	-88.31	0.33	N1'	-244.84
N6'H	7.50	C8	163.37	-16.69	0.47	N3'	-277.29
C7H	4.73	C11	136.05	-5.02	0.49	N5'	-298.66
C8H	9.28	C10	157.85	-46.21	0.68	N4'	-333.91
C5H	8.17	C3	136.03	-68.94	0.45	N6'	-361.15
C3H	7.04	C4	134.07	-62.88	0.51		
C9H	6.13	C5	136.01	-88.48	0.57		
C12H	3.45	C6	104.09	-73.23	0.31		
C19H	4.22	C2	117.04	-104.62	0.56		
C13H	4.06	C9	65.79	-82.31	0.39		
C16H	2.92	C13	58.14	-54.04	0.42		
C15H	3.80	C18	48.95	-37.44	0.45		
C18H	3.36	C17	77.66	-57.03	0.56		
C14H	3.60	C12	50.37	-81.37	0.52		
C17H	2.68	C15	49.61	-60.70	0.58		
		C14	42.56	-123.46	0.63		
		C19	69.23	-101.97	0.56		
		C16	40.35	-26.68	0.50		

Table S11: NMR chemical shifts of virtual structure **5**, from CASTEP calculation (chemical shielding references: σ_{ref}^{1H}=31.04; σ_{ref}^{13C}=169.55; σ_{ref}^{15N}=-161.64).

2.2.6. Virtual crystal 6a

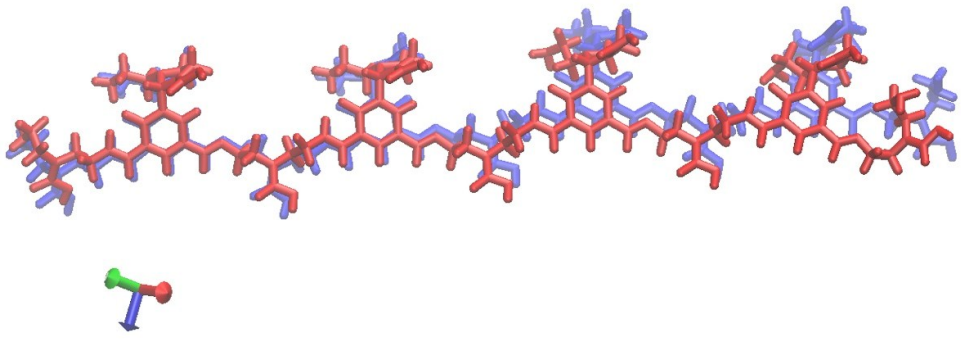

Figure S20: molecular model of the oligodynablock corresponding to virtual crystal **6a** before (blue) and after (red) QM refinement

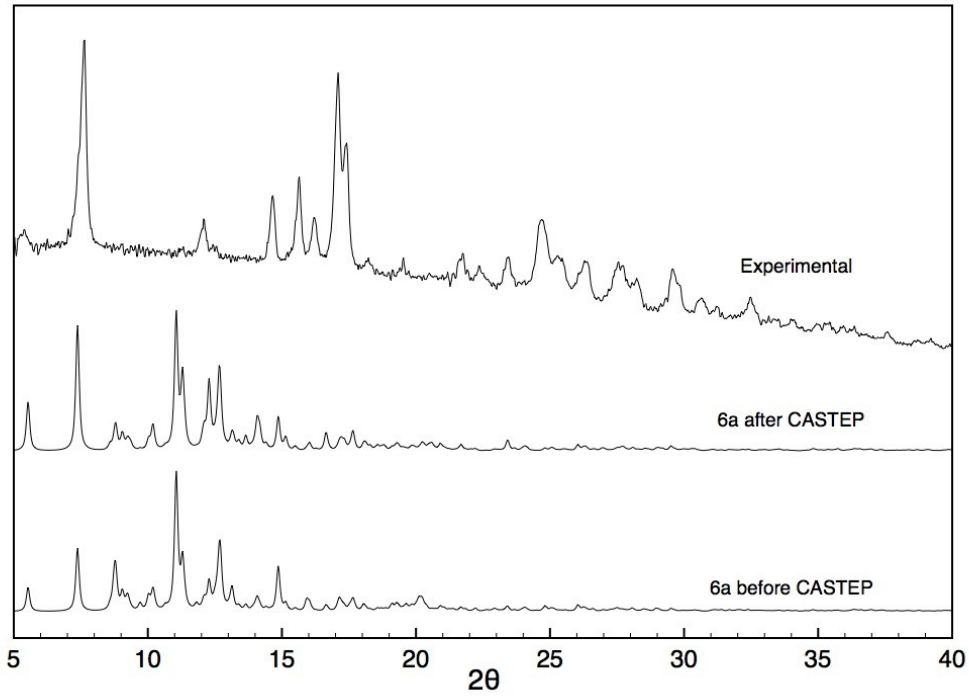

Figure S21 : PXRD spectrum of virtual crystal **6a** before and after QM refinement

^{1}H	δ (ppm)	^{13}C	δ_{iso} (ppm)	Aniso (ppm)	Asymmetry	^{15}N	δ (ppm)
C10OOH	5.50	C1	179.86	-153.03	0.23	N2'	-59.79
N1'H	15.83	C7	159.40	-134.92	0.76	N1'	-239.70
N6'H	6.24	C8	162.25	137.38	0.50	N3'	-280.18
C7H	8.35	C11	152.30	115.34	0.15	N5'	-298.79
C8H	9.55	C10	151.80	130.36	0.17	N4'	-334.12
C5H	8.08	C3	136.08	-157.57	0.73	N6'	-361.01
C3H	7.49	C4	133.61	-156.36	0.39		
C9H	6.70	C5	129.90	-189.05	0.68		
C12H	3.81	C6	122.51	-166.10	0.40		
C19H	4.50	C2	114.00	-167.70	0.24		
C13H	4.26	C9	67.40	-0.80	0.86		
C16H	3.54	C13	57.27	-67.44	0.37		
C15H	4.03	C18	45.98	-54.60	0.93		
C18H	3.68	C17	46.88	-61.06	0.63		
C14H	3.84	C12	47.65	-51.63	0.45		
C17H	2.80	C15	44.95	-54.98	0.33		
		C14	42.07	-61.53	0.57		
		C19	41.96	-37.22	0.74		
		C16	36.62	-42.78	0.66		

Table S13: NMR chemical shifts of virtual structure **6a**, from CASTEP calculation (chemical shielding references: σ_{ref}^{1H}=31.24; σ_{ref}^{13C}=166.35; σ_{ref}^{15N}=-157.92).

2.2.7. Virtual crystal 6b

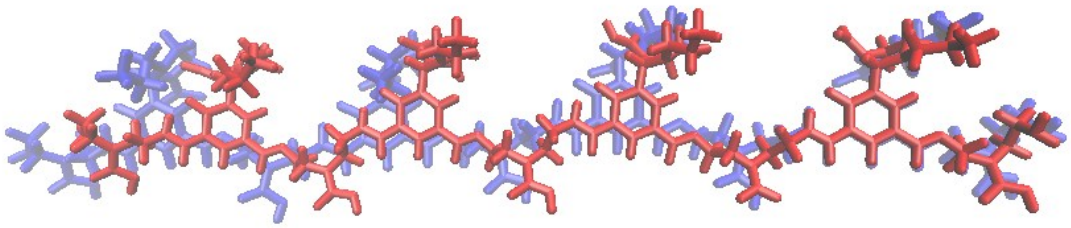

Figure S22 : molecular model of the oligodynablock corresponding to virtual crystal **6b** before (blue) and after (red) QM refinement

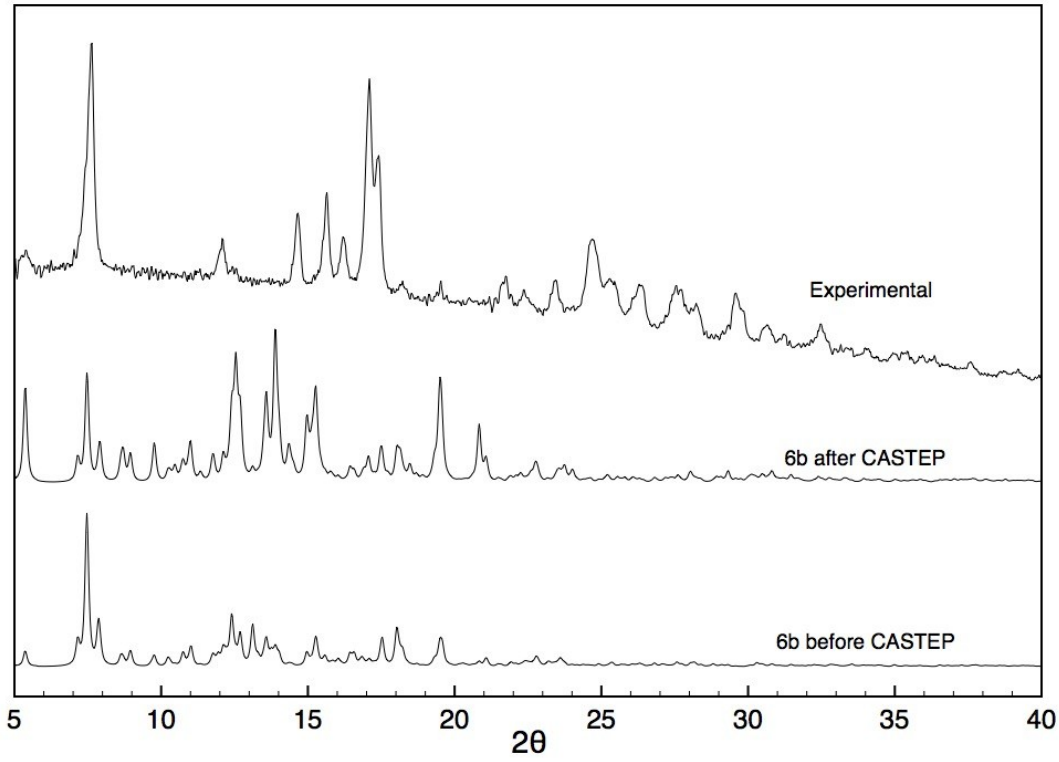

Figure S23: PXRD spectrum of virtual crystal **6b** before and after QM refinement

^{1}H	δ (ppm)	^{13}C	δ_{iso} (ppm)	Aniso (ppm)	Asymmetry	^{15}N	δ (ppm)
C10OOH	14.37	C1	181.37	-146.92	0.47	N2'	-54.92
N1'H	13.69	C7	154.70	-87.85	0.61	N1'	-268.43
N6'H	8.99	C8	162.92	137.82	0.56	N3'	-275.88

C7H	7.15	C11	162.16	56.32	0.55	N5'	-302.07
C8H	8.72	C10	158.79	100.49	0.52	N4'	-308.58
C5H	7.70	C3	136.56	-150.50	0.40	N6'	-363.76
C3H	6.51	C4	140.99	-155.42	0.61		
C9H	6.00	C5	132.40	-188.83	0.37		
C12H	2.85	C6	126.24	-167.52	0.49		
C19H	3.82	C2	118.56	-166.76	0.75		
C13H	3.51	C9	77.37	-59.08	0.52		
C16H	2.98	C13	60.31	-70.67	0.63		
C15H	3.26	C18	51.18	-40.15	0.57		
C18H	3.11	C17	51.29	-54.84	0.43		
C14H	2.66	C12	45.19	-49.52	0.59		
C17H	2.88	C15	43.49	-48.75	0.70		
		C14	42.68	-5.57	0.49		
		C19	46.37	1.30	0.72		
		C16	38.28	-22.44	0.56		

Table S15: NMR chemical shifts of virtual structure **6b**, from CASTEP calculation (chemical shielding references: σ_{ref}^{1H}=30.5; σ_{ref}^{13C}=169.25; σ_{ref}^{15N}=-167.6).

Figure S23: PXRD spectrum of virtual crystal **6b** before and after QM refinement

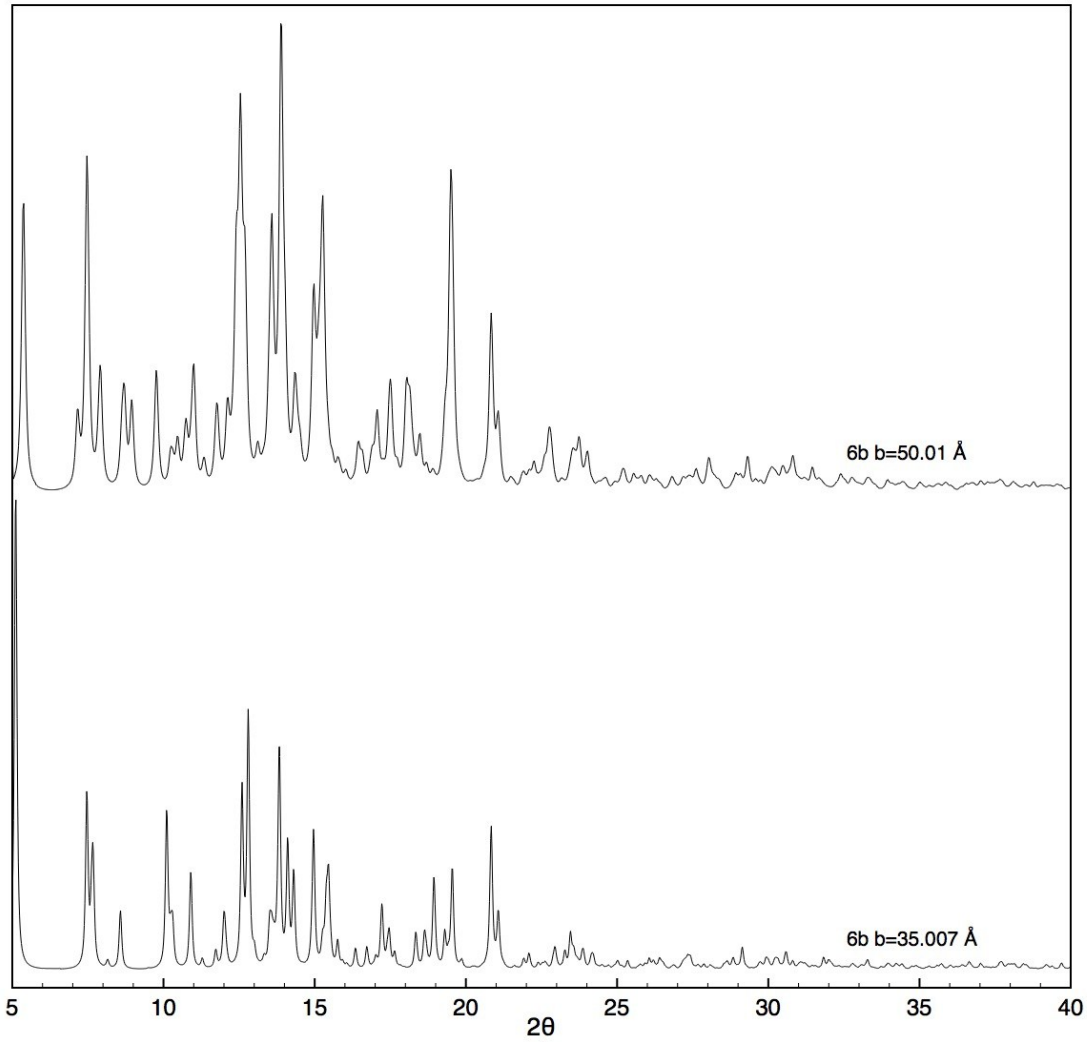

Figure S24: Predicted PXRD pattern for crystal **6b** observed for the full predicted unit cell (upper trace) and by removing some empty space (which may contain water) (lower trace). The latter is obtained by changing the unit cell dimensions along the b direction (from 35.007 to 50.01 Å) while keeping the atomic coordinates fixed.

2.2.8. Virtual crystal 6c

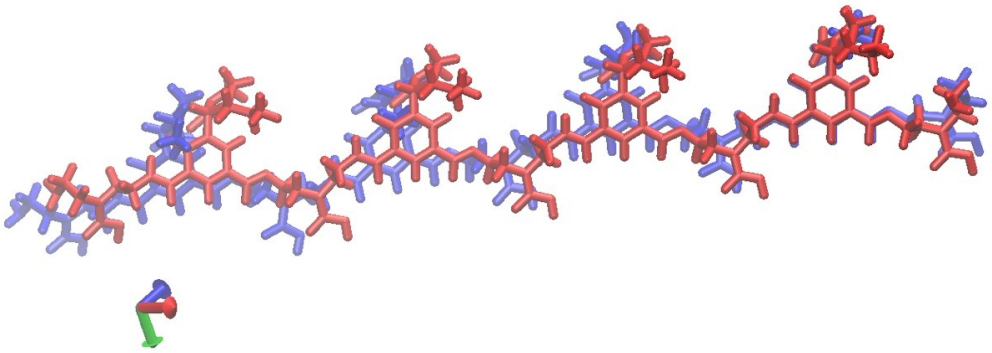

Figure S25 : molecular model of the oligodynablock corresponding to virtual crystal **6c** before (blue) and after (red) QM refinement

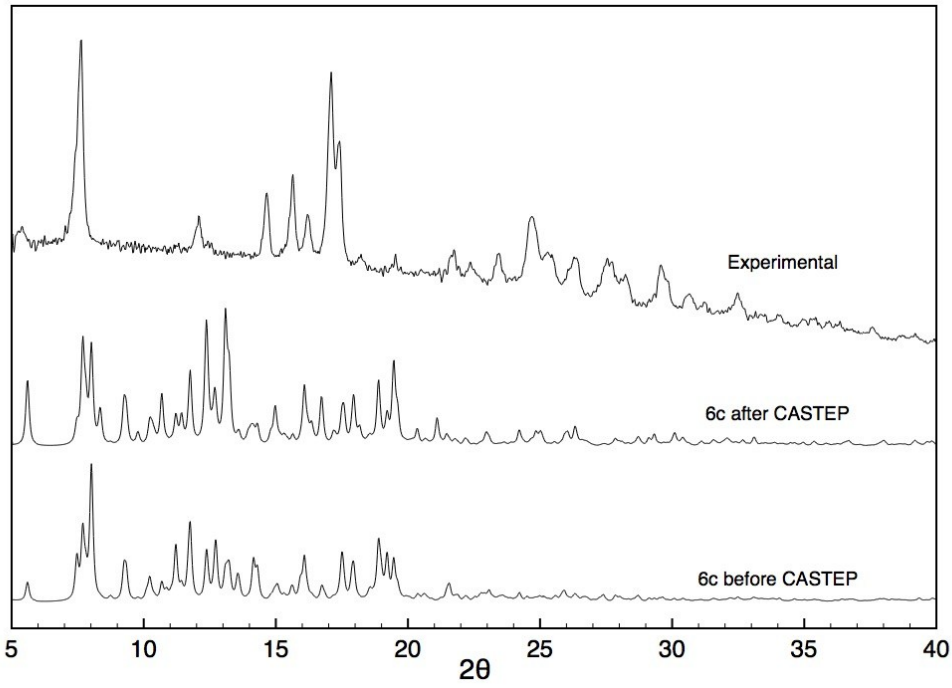

Figure S26 : PXRD spectrum of virtual crystal **6c** before and after QM refinement

^{1}H	δ (ppm)	^{13}C	δ_{iso} (ppm)	Aniso (ppm)	Asymmetry	^{15}N	δ (ppm)
C10OOH	11.08	C1	182.48	-138.53	0.22	N2'	-51.58

N1'H	12.97	C7	152.61	-112.62	0.51	N1'	-272.54
N6'H	8.77	C8	162.65	110.24	0.50	N3'	-254.72
C7H	7.25	C11	161.41	99.29	0.63	N5'	-299.49
C8H	9.17	C10	158.29	109.47	0.25	N4'	-330.68
C5H	8.29	C3	134.85	-132.48	0.53	N6'	-364.57
C3H	6.79	C4	150.41	-167.00	0.45		
C9H	6.16	C5	131.10	-173.68	0.82		
C12H	3.37	C6	126.02	-151.08	0.51		
C19H	4.22	C2	119.64	-155.53	0.55		
C13H	4.11	C9	75.56	58.05	0.63		
C16H	2.74	C13	60.02	-76.49	0.59		
C15H	3.55	C18	50.69	15.08	0.77		
C18H	3.81	C17	45.90	62.74	0.70		
C14H	3.21	C12	45.62	-54.61	0.61		
C17H	2.86	C15	45.08	-61.88	0.51		
		C14	44.30	-23.08	0.92		
		C19	47.07	-55.17	0.69		
		C16	37.13	52.40	0.66		

Table S17: NMR chemical shifts of virtual structure **6c**, from CASTEP calculation (chemical shielding references: σ_{ref}^{1H}=27.45; σ_{ref}^{13C}=166.17; σ_{ref}^{15N}=-170.09).

2.3. Assessment of the generated virtual crystals

Structure	^{1}H δ_{iso} rmsd[a] (ppm)	^{15}N δ_{iso} rmsd[a] (ppm)	^{13}C δ_{iso} rmsd[a] (ppm)	^{13}C δ_{aniso} rmsd[a] (ppm)	E[c] (kcal/mol)
1	2.37	16.1	6.25	-	-142
2a	1.33	16.1	4.28	24.5	-188
2b	1.1	18	4.92	101	-187
3	1.16	16.1	3.87	15.4	-140
5	1.56	17.0	11.9	83.3	-117
6a	2.44	15.1	4.87	18.2	-187
6b	0.58	25.2	4.84	27.0	-208
6c	0.91	28.7	6.06	47.0	-186

[a] Root mean square deviation between experimental and calculated NMR chemical shift tensor parameters.
[b]Calculated energy of the geometry optimized crystal structure.
Abnormally high values are underlined.

Table S18: Five different parameters of the model crystal structures **1**-**6** used to assess the quality of the structures.

References

(1) Z. Guo, P. J. Sadler, and E. Zang, *Chem. Commun.*, 1997, 27.
(2) J. Leclaire, G. Husson, N. Devaux, V. Delorme, L. Charles, F. Ziarelli, P. Desbois, A. Chaumonnot, M. Jacquin, F. Fotiadu, and G. Buono. *J. Am. Chem. Soc.* 2010, **132**, 3582.
(3) M. Rosay, L. Tometich, S. Pawsey, R. Bader, R. Schauwecker, M. Blank, P. M. Borchard, S. R. Cauffman, K. L. Felch, R. T. Weber, R. J. Temkin, R. G. Griffin, and W. E. Maas, *Phys. Chem. Chem. Phys.* 2010, **12**, 5850.
(4) C. S. Song, K. N. Hu, C. G. Joo, T. M. Swager, and R. G. Griffin, *J. Am. Chem. Soc.* 2006, **128**, 11385.
(5) O. Peersen, X. Wu, I. Kustanovich, and S. Smith, *J. .Magn. Reson. Series A* 1993, **104**, 334.
(6) A. Zagdoun, G. Casano, O. Ouari, M. Schwarzwälder, A. J. Rossini, F. Aussenac, C. Copéret, A. Lesage, P. Tordo, and L. Emsley, L. *J. Am. Chem. Soc.* 2013, **135**, 12790..
(7) P. C. A. van der Wel,; K. N. Hu, J. Lewandowski, and R. G. Griffin, *J. Am. Chem. Soc.* 2006, **128**, 10840.
(8) A. J. Rossini, A. Zagdoun, F. S. Hegner, M. Schwarzwälder, D. Gajan, C. Copéret, A. Lesage, and L. Emsley, *J. Am. Chem. Soc.* 2012, **134**, 16899.
(9) B. M. Fung, A. K. Khitrin, and K. Ermolaev, *J. Magn. Reson.* 2000, **142**, 97.
(10) G. Pèpe, and D. Siri, In *Modeling of Molecular Structures and Properties Studies in Physical and Theoretical Chemistry*; Rivail, J. L., Eds.; Elsevier B. V.: Amsterdam, 1990.
(11) G. Del Re, *J. Chem. Soc.* 1958, **40**, 4031.
(12) G. Pèpe, B. Serres, D. Laporte, G. Del Re, and C. Minichino, *J. Theor. Biol.* 1985, **115**, 571.
(13) A. L. Spek, *J. Appl. Crystallogr.* 2003, **36**, 7.
(14) S. J. Clark, M. D. Segall, C. J. Pickard, P. J. Hasnip, M. J. Probert, K. Refson, and M. C. Payne, *Z. Kristallogr.* 2005, **220**, 567.
(15) J. P. Perdew, K. Burke, and M. Ernzerhof, *Phys. Rev. Lett.* 1996, **77**, 3865.
(16) D. Vanderbilt, *Phys. Rev. B* 1990, **41**, 7892.
(17) H. J. Monkhorst, and J. D. Pack, *Phys. Rev.* B 1976, **13**, 5188.
(18) C. J. Pickard, and F. Mauri, *Phys. Rev.* B 2001, **63**, 245101.
(19) J. Schaefer, E. O Stejskal, J. R Garbow, and R. A McKay, *J. Magn. Reson.* 1984, **59**, 150.
(20) J. Z. Hu, D. W. Alderman, C. H. Ye, R. J. Pugmire, and D. M. Grant, *J. Magn. Reson. Ser. A* 1993, **105**, 82.